Optimization of investment casting process for K477 superalloy aero-engine turbine nozzle by simulation and experiment

Xin Hao[1, 2], Guo-huai Liu[3], *Ye Wang[4], Shi-ping Wu[5], and Zhao-dong Wang[3]

1. AECC South Industry Company Limited, Zhuzhou 412002, Hunan, China
2. State Key Laboratory of Solidification Processing, Northwestern Polytechnical University, Xi'an 710072, China
3. State Key Laboratory of Rolling and Automation, Northeastern University, Shenyang 110819, China
4. School of Materials Science and Chemical Engineering, Harbin University of Science and Technology, Harbin 150001, China
5. School of Materials Science and Engineering, Harbin Institute of Technology, Harbin 150001, China

Abstract: In order to reduce the shrinkage porosity of nickel-based superalloy castings in the investment casting process, the effects of different gating systems on mold filling, solidification process, and prediction of shrinkage porosity of aero-engine turbine nozzle castings were investigated by simulation and experimental methods. Results show that the design of the vertical runner would cause greater turbulence of the melt in the riser during the mold filling process, and the outer runner is not necessary. With the decrease in number of runners, the hot spot moves down towards the casting, and the shrinkage and porosity defects are formed in the casting below the riser. In the original designs, a certain tendency of shrinkage and porosity defect is found in the vanes, inner rings, and outer rings of the castings by both simulation prediction and experiment. Finally, based on the processing optimization, the aero-engine turbine nozzle casting with no shrinkage and porosity defects is obtained.

1 Introduction

As a key component in aero-engine, the turbine nozzle works under great and complex stress in the temperature range of 700 °C to 1,100 °C [1-3]. Therefore, nickel-based superalloys with good oxidation, creep resistance, high stability, and excellent strength [4-6] are often used in the manufacture of the turbine nozzle. However, the turbine nozzle has a complex frame structure, including inner cone, inner ring, blades, outer ring, and flange. Furthermore, the wall thickness of each part is greatly different, especially the thickness of the blades, which is only a few millimeters [7-9]. Although the vacuum investment casting process is applied in the production of nickel-based superalloys turbine parts, which can achieve the nominal casting dimensions by

an appropriate degree of accuracy of wax pattern, and can ensure the consistency of the blade and the overall dimensional accuracy of the parts [10-13], the defects, including shrinkage porosity and crack are still easily induced during the solidification process and extremely difficult to remove [14-18].

It is worth noting that both the design of the gating system and the casting process parameters are always considered as the most important factors which affect casting quality because the solidification sequence and behavior of castings can be changed by controlling the relevant parameters [19-23]. Moreover, the different casting shapes and alloy types also lead to significant variations in the design of the gating systems, which usually depending on the engineer's experiences with trials and errors practice. Therefore, to determine the appropriate casting design for complex structures of castings in a rapid, reliable, and economic fashion, it is very important to predict the defects and minimize the number of trials and errors experiments by simulation at the design stage [24-26].

In the current study, based on a combined analysis of flow transfer and heat transfer, the gating systems

*Ye Wang

Male, Ph.D. His research interests mainly focus on numerical simulation of heat and mass transfer and defect predication during the mould filling and solidification process of metal melt.

E-mail: ohenry1980@163.com

of nickel-based superalloy aero-engine turbine nozzle castings are optimized and the shrinkage porosity defects are predicted by the simulation of the investment casting process. Finally, the optimal design of the gating system of aero-engine turbine nozzle castings is proposed and verified by the trial manufacture.

2 Simulation and experiment procedures

2.1 Experiment material

The casting alloy employed in the present study was the K477 nickel-based superalloy, a typical martensite precipitation reinforced alloy, which has good comprehensive mechanical properties with the nominal composition shown in Table 1. The thermal physical parameters of the K477 superalloy for simulation, such as phase transition temperature, latent heat of crystallization, thermal conductivity, and specific heat, were measured in the National Nonferrous Metal and Electronic Materials Analysis and Testing Center. A complete set of obtained material thermophysical properties at the range of solidus temperature to 1,535 °C are listed in Table 2. Due to the experimental data of some thermophysical properties in the solid-liquid two-phase region of 1,232.17 °C to 1,311.63 °C being unavailable, the thermodynamic databases in ProCAST were used to obtain the properties of K477 alloy in the temperature range of 1,232 °C to 1,535 °C as well as in other relevant studies [14, 23, 25], such as enthalpy curve, the solidification path, density, viscosity and thermal conductivity. The calculated properties of density and conductivity are well coincident with the experimental data, as shown in Fig. 1.

Table 1: Nominal composition of K477 superalloy (wt.%)

Cr	Co	Al	Ti	Mo	C	Fe	B	Ni
14.78	15.30	4.34	3.51	0.14	0.08	≤0.5	≤0.02	Bal.

Table 2: Thermophysical properties of K477 superalloy

| Temperature (°C)	Conductivity (W·m^{-1}·K^{-1})	Viscosity (Centipoise)	Density (kg·m^{-3})	Enthalpy (kJ·kg^{-1})
1,232	21.43	-	7,719.41	832.706
1,262	21.53	10.05	7,702.60	844.217
1,282	22.29	9.52	7,661.57	880.972
1,303	23.18	9.08	7,606.19	935.740
1,323	24.49	9.08	7,536.70	1,008.472
1,342	26.46	8.46	7,444.82	1,110.226
1,375	26.96	7.90	7,412.68	1,155.116
1,415	27.36	6.72	7,381.98	1,184.038
1,455	27.75	6.22	7,351.25	1,213.503
1,495	28.14	5.78	7,320.47	1,243.262
1,535	28.52	5.73	7,289.64	1,273.264
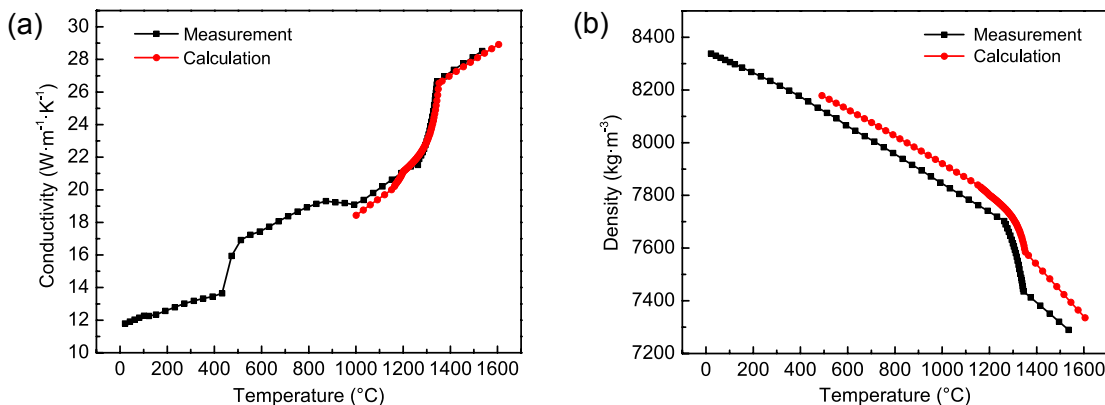
Fig. 1: Thermal properties of K477 alloy: (a) conductivity; (b) density

2.2 Casting process and design

Zircon and fused silica were employed for the preparation of the shell mold, and the shell mold was composed of the following nine coatings: a zircon prime face coating, two intermediate coatings, five backup coatings, and one seal coating. Furthermore, each coating contained one slurry layer and one stucco layer, and the thickness of the shell mold was approximately 9±0.5 mm. The molds were preheated in a furnace in two steps. The first step was to sinter the molds at a temperature of 950±5 °C. Then, the temperature was raised to 1,100±5 °C and held for 2 h to equalize the temperature distribution in the shell mold for subsequent pouring. The K477 alloy was melted in the vacuum induction melting furnace and poured at 1,450±10 °C into the shell mold in a vacuum of $1×10^{-2}$ Pa.

A three-dimensional CAD model of the turbine nozzle was created and is shown in Fig. 2(a). It can be observed that there are many turbine vanes with thin-walled structures connected to the cylindrical shell structure, as illustrated in Fig. 2(b). The thickness of these is between 1 mm to 2 mm. Any defects will lead the turbine nozzle to be directly scrapped because the turbine vanes cannot be machined. Obviously, there is a great tendency of shrinkage porosity at the connecting part induced by the inconsistent cooling rate of castings due to the large wall thickness difference, which seriously affects the casting quality. Thus, the main difficulty of the aero-engine turbine nozzle manufactured by investment casting is to overcome the tendency of shrinkage porosity of the casting.
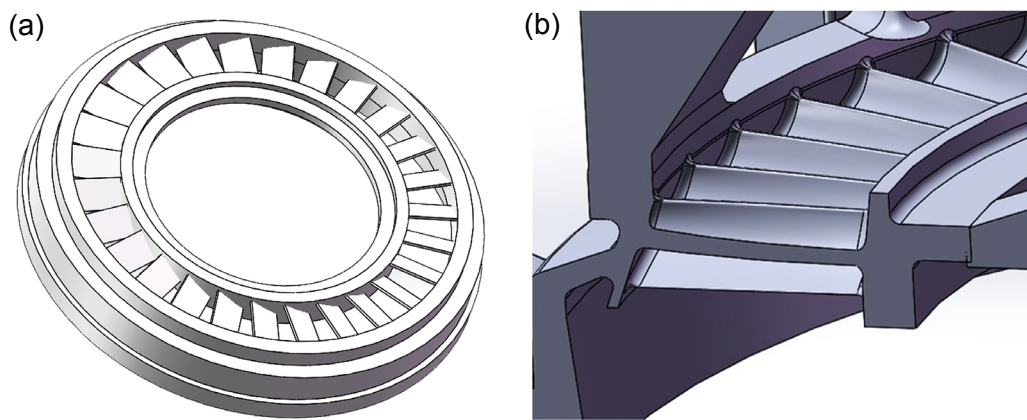

(a)   (b)

Fig. 2: Three-dimensional model of turbine nozzle casting (a) and cross-section of vanes (b)

According to the analysis of the turbine nozzle structure described above, the gating system was designed to ensure the complete filling and effective feeding in the casting, as shown in Fig. 3(a). As a contrast, the Scheme 2 gating system was designed by reducing the number of runners to investigate the feeding efficiency of the corresponding riser, as shown in Fig. 3(b). In addition, in order to reduce the volume of the gating system and increase the technological yield of the casting, the gating system was modified under the consideration of feeding distance of the casting, as shown in Fig. 3(c). The uniform finite element mesh was created in the MeshCast module of ProCAST, the mesh length range of the casting was between 1 mm to 5 mm, and that of gating system was between 5 mm to 20 mm, as illustrated in Figs. 4(a) to (c). Shell molds of the castings were created and meshed using the shelling feature in MeshCAST, as shown in Figs. 4(d) and (e). The shrinkage and porosity were predicted and counted by calculating the packing pressure on the casting and the pressure drop within the mushy zone during solidification in the Advanced Porosity Model (APM) module of ProCAST.
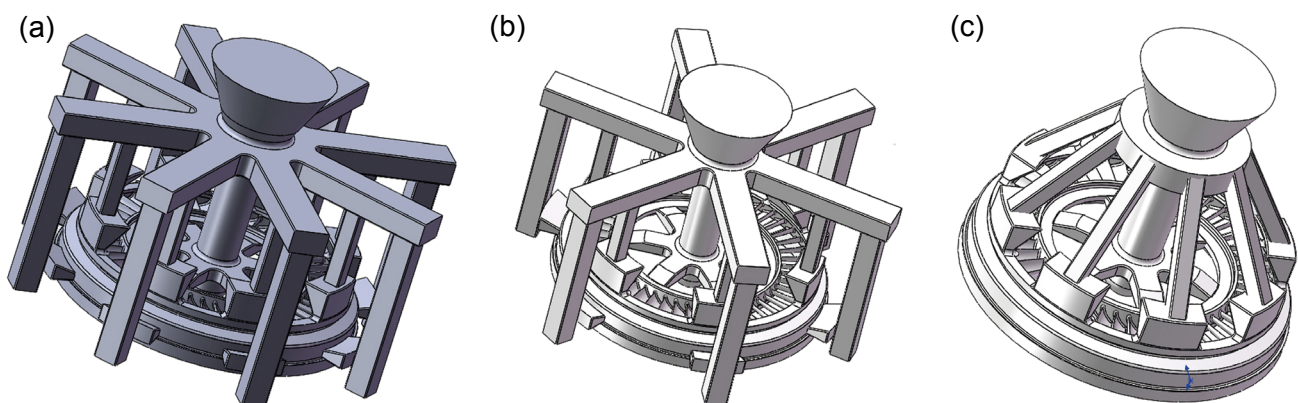

(a)   (b)   (c)

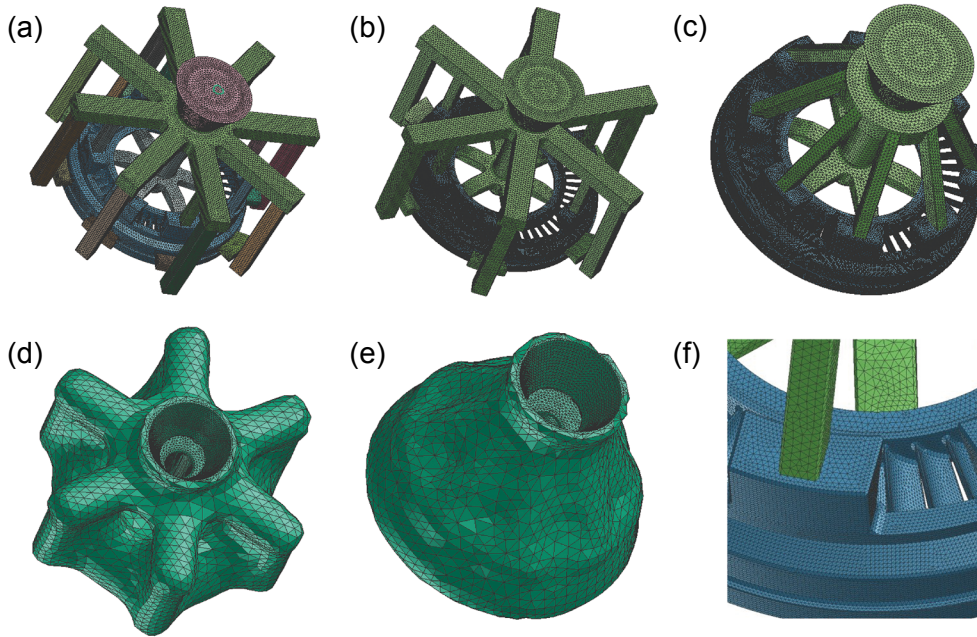Fig. 3: Different process design schemes of turbine nozzle casting

Fig. 4: Finite element mesh of turbine nozzle casting with different gating systems (a)–(c), meshes of casting mold shell (d) and (e), and local details of the non-uniform mesh (f)

3 Results and discussion

3.1 Filling process

The simulation results of the mold filling at the pouring time of 2 s are shown in Fig. 5. The temperatures of the melt under three kinds of casting processes are all higher than the liquidus temperature, which indicates that there is enough degree of superheat for the mold filling. Meanwhile, the filling rate of the top horizontal runner both in Scheme 1 and Scheme 2 is slower than the tilting runner in Scheme 3, as shown in Figs. 5(a) to (c). Moreover, the horizontal runner at the bottom is already filled and the

Fig. 5: Melt distribution at filling time of 2 s under three process schemes: (a) Scheme 1; (b) Scheme 2; (c) Scheme 3

vanes connecting the runner are almost completely filled in Scheme 1 and Scheme 2, where is not filled in Scheme 3. This means that the order of melt velocity of mold filling at this position is Scheme 1, Scheme 2 and Scheme 3.

To identify the mold filling behavior in the risers of three schemes clearly, the melt velocity-time curves at different positions are plotted in Fig. 6, and the corresponding positions of the selected points are marked in Fig. 6(a). Apparently, because the volume of the gating system in Scheme 3 is the smallest, it can be seen that the melt filling velocity is more stable than other schemes in the vanes and riser of Scheme 3, which means that the filling process of Scheme 3 is smoother and steadier. The filling time at different positions along the filling direction is listed in Table 3. The melt flows from Point A to Point B in the casting, while the melt flows into the inner vertical runner and the riser with the filling sequence of D to C in all schemes, which indicates that the riser is filled with melt from the runner and casting until the melt meets at Point C.

More important, for Scheme 1 and Scheme 2, the filling sequence of the outer runners is from B to F as the filling time of Point F is much longer than that of Point E and Point B, which indicates that the casting has already been completely filled when the riser begins to fill. Therefore, the design of the outer runner is completely unnecessary, especially in combining the results of filling behavior of the melt in the riser shown in Fig. 7, which suggests that the design of the vertical runner would lead to the formation of greater turbulence of the melt
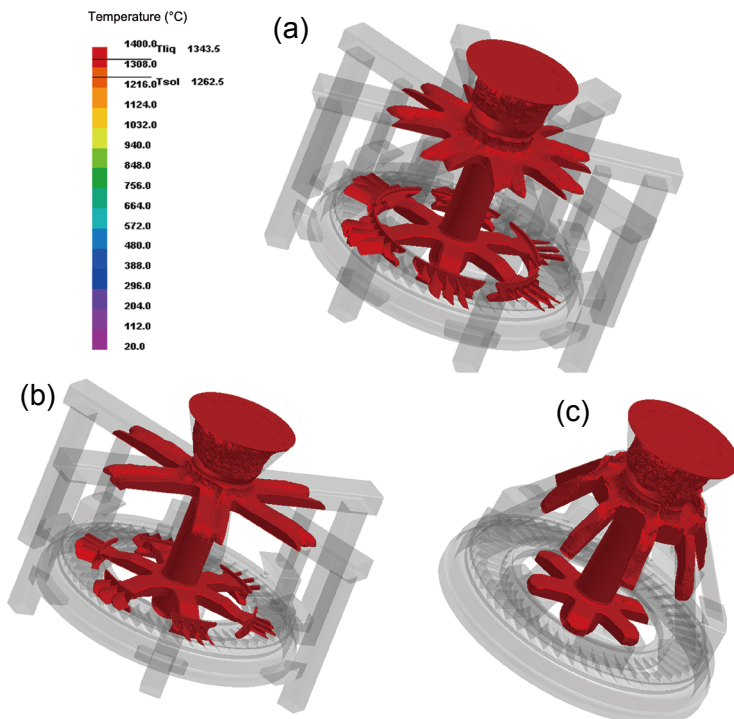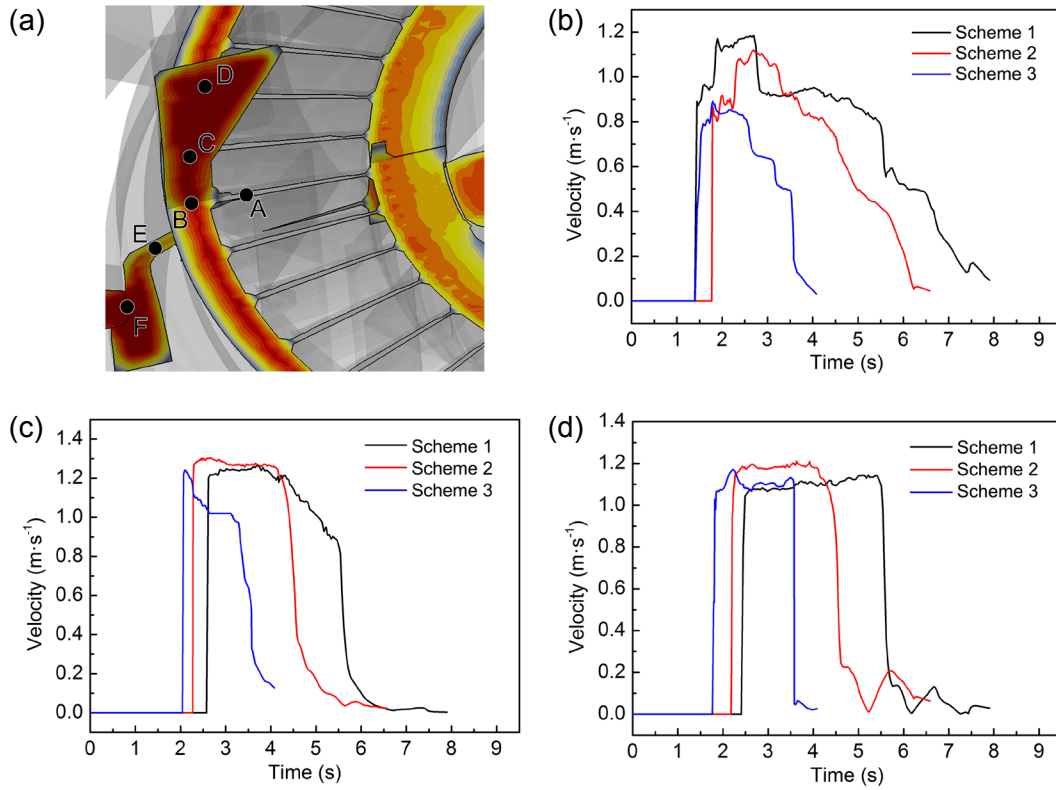
Fig. 6: Filling velocity of three process schemes at selected positions in (a): (b) Point A; (c) Point B and (d) Point C

Table 3: Filling time (s) at different points along the filling direction as marked in Fig. 6(a)

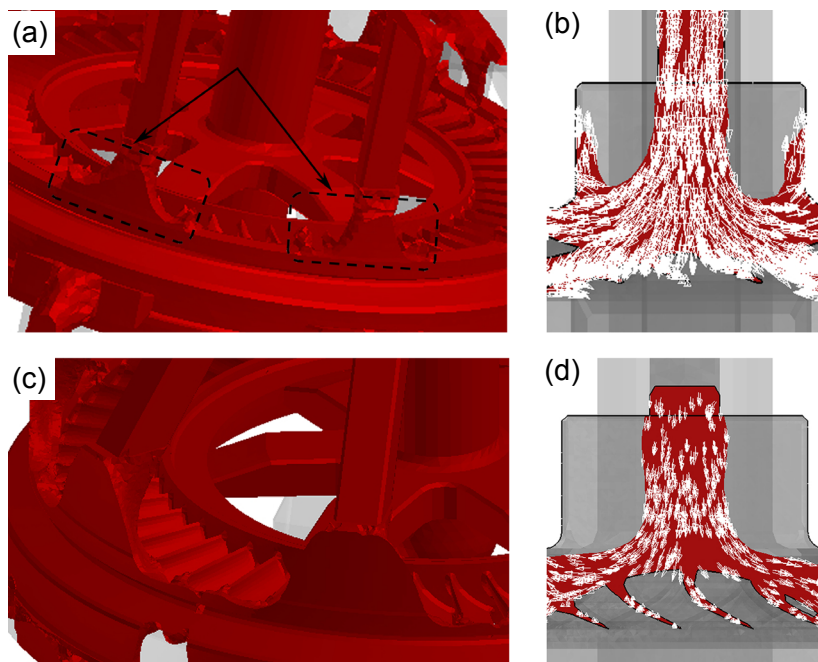| Schemes	Points					
	A	B	C	D	E	F
1	1.728	2.335	2.595	2.385	2.473	3.060
2	1.406	2.071	2.287	2.226	2.585	3.316
3	0.921	1.529	2.154	2.135	-	-

Fig. 7: Filling behavior of melt in risers: (a), (b) turbulence in Scheme 1 and Scheme 2; (c), (d) laminar in Scheme 3

in the riser during the filling process. That would have a great impact on the final quality of the casting. Therefore, the design of Scheme 3 is the best choice due to the reasonable filling sequence, stable filling process, and justified filling velocity by the analysis of the above factors.

3.2 Solidification process

Figure 8 shows the simulation results of the cooling curve along the feeding path of the vanes which are facing the riser

in three schemes. The selected Points A to E along the feeding path are marked in Fig. 8(a). From Figs. 8(b)–(d), it can be observed that there is a good solidification sequence at the vanes in three schemes at the beginning of solidification. However, the temperature gradient of the feeding path of Scheme 2 almost disappears when the melt cools into the temperature range between the liquidus and solidus. That would cause a great tendency of shrinkage and porosity in the vanes and their connective positions between the inner and outer rings.
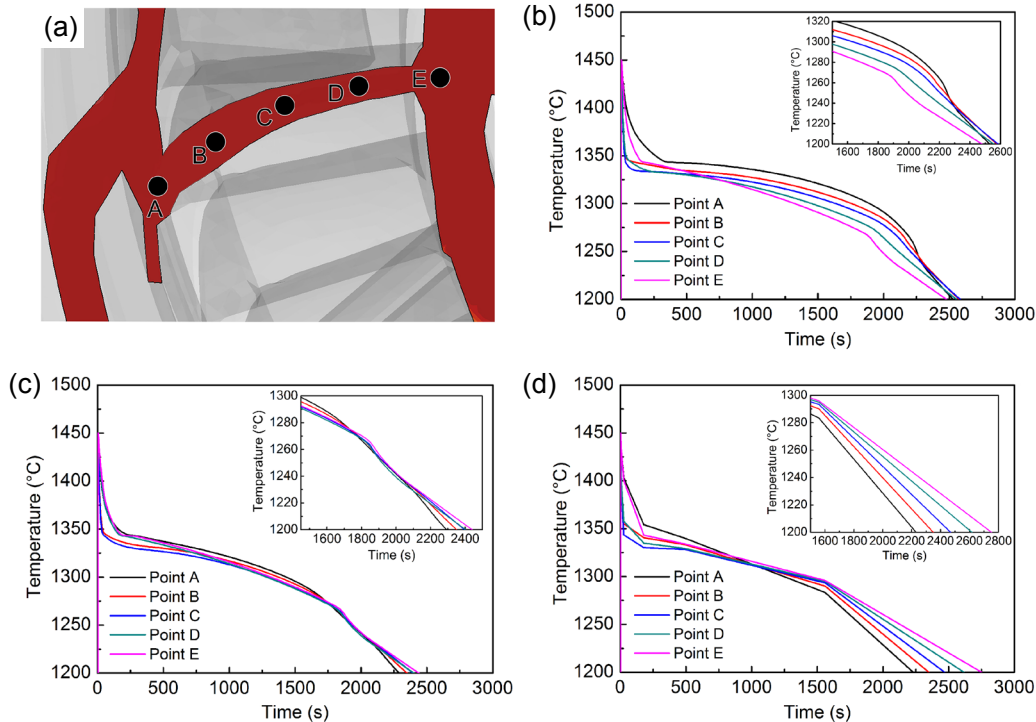

Fig. 8: Cooling curves of points along the feeding path of vanes (a) in different schemes: (b) Scheme 1; (c) Scheme 2; (d) Scheme 3

Although the temperature gradient on the vanes in Schemes 1 and 3 is reasonable and uniform, it is still too low to establish a good feeding sequence adequately in Scheme 1 from the results shown in Fig. 8(b). To clarify this further, the feeding angle of the vanes at 1,552 s after filling was investigated by the results of the solid fraction, as contoured in Figs. 9(a) to (c). Obviously, the feeding angle between 30º to 45º is too small to achieve effective feeding, which indicates that the vanes and its ends still have a certain shrinkage porosity tendency in Scheme 1. From a result shown in the Fig. 9(d), it can be seen that the feeding angle in the vanes is almost straight (close

to 180º), which suggests the vanes can be effectively fed. Moreover, the thermal effect between risers will be diminished due to the reduction in the number of the risers from eight to six, thus, the solidification time of the riser becomes shorter, which also results in a hot spot moving down into the casting and accelerates cooling of the casting part between risers. As a consequence, the tendency of shrinkage and porosity of the casting below riser is increased. Through the analysis of the solidification results, including temperature gradient, feeding angle, and feeding effect of riser, the Scheme 3 should be the most ideal among the three schemes.
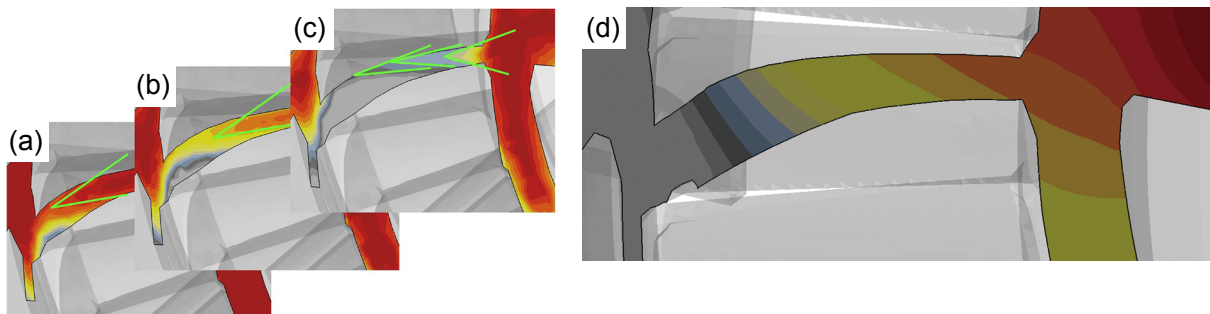

Fig. 9: Solid fraction distribution and feeding angle on the vane of Scheme 1 (a–c) at different times and Scheme 3 (d)

3.3 Shrinkage and porosity prediction

Based on the analysis of the simulation results of the filling and solidification processes under different gating system schemes, it is not difficult to determine the location of shrinkage and porosity in the turbine nozzle castings. For the Scheme 1, both the inner and outer cylindrical shell and turbine vanes have great forming tendency of shrinkage and porosity, and for Scheme 2, the shrinkage and porosity defects are more likely to occur at the top of the turbine vanes and at the outer cylindrical shell below the riser. The prediction of the tendency and locations of shrinkage porosity defects indicates

that the result of APM module calculations accord with the analysis, as illustrated in Fig. 10. Comparison of the tendency of shrinkage and porosity in Schemes 1, 2, 3 indicates that the reduction of riser will cause the solidification inhomogeneity of the outer cylindrical shell and hence weaken the feeding effect. According to the prediction results of shrinkage and porosity of Scheme 3 shown in Fig. 10(c), only a few porosity defects are found inside the turbine vanes with a certain probability of occurrence between 2.5% and 0.5%. Therefore, Scheme 3 is the best choice among the three casting processes.
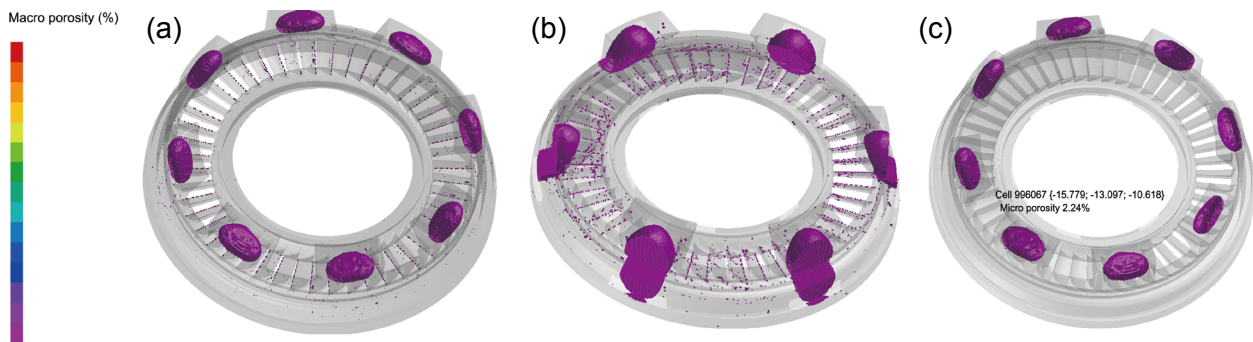

Fig. 10: Prediction of shrinkage and porosity defects on castings of different schemes: (a) Scheme 1; (b) Scheme 2; (c) Scheme 3

4 Experimental validation

Figure 11 shows the observation results of the shrinkage porosity defects in castings by Schemes 1 and 3 manufactured under the same process parameters. Fluorescent penetrant inspection was conducted for observation of the morphology and location of shrinkage and porosity. The defects of misrun

appear at the top of some turbine vanes and much shrinkage porosity appear at the connective position between turbine vanes and cylindrical shell in the casting by Scheme 1, as shown in Fig. 11(a) and Fig. 12(a). Two results, as shown in Fig. 11(b) and Fig. 12(b) confirm that no misrun, shrinkage porosity and other defects are found in the casting by Scheme 3, which accords with the predicted results.
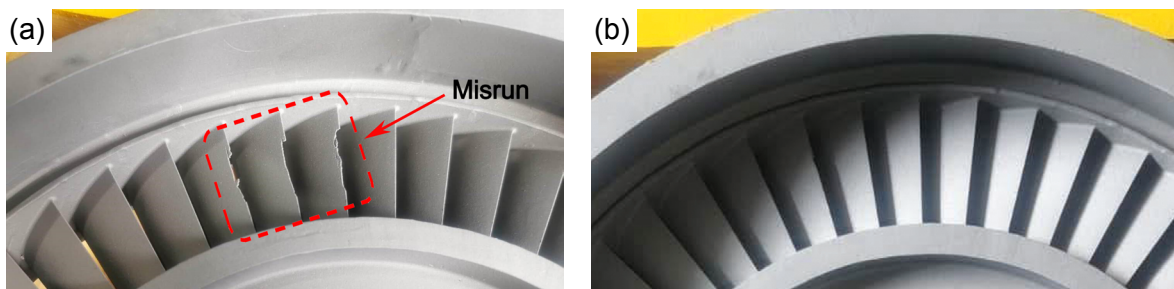

Fig. 11: Shrinkage and porosity defects observed in confirmed experiments: (a) Scheme 1; (b) Scheme 3
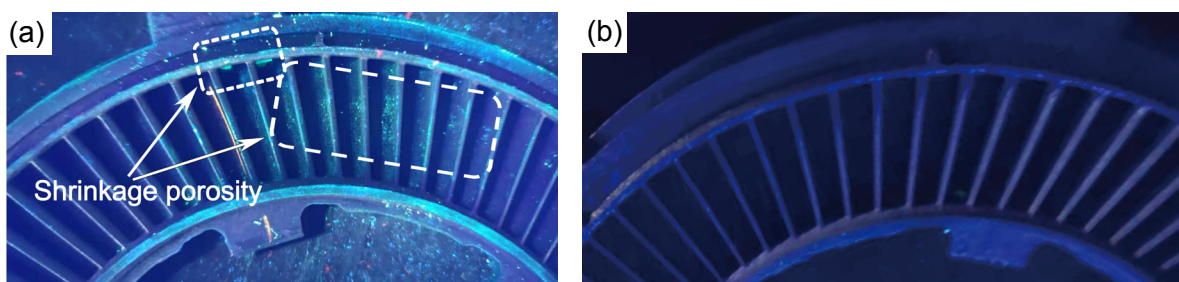

Fig. 12: Shrinkage and porosity defects detected by fluorescent penetrant inspection on castings of different schemes: (a) Scheme 1; (b) Scheme 3

5 Conclusions

(1) The melt is filled backward from the casting to the outer runner in Schemes 1 and 2, which suggests that the outer runner is unnecessary. The design of the vertical runner causes the melt to flow into the riser with high speed and induces a greater turbulence of the melt in the riser during the filling process. In contrast, the sloped runner can effectively reduce flow speed of the melt in the risers, and allows for a more stable filling process. Compared with Schemes 1 and 2, the process of Scheme 3 has a reasonable filling sequence in the turbine vanes.

(2) The temperature gradient of the vanes in Scheme 2 and the feeding angle of the vanes in Scheme 1 are both very low during the solidification process, which induce a great tendency of shrinkage porosity formation in the vanes and their ends on both sides. The solid fraction results further show that the hot spot moves down towards the casting when the number of risers decrease, hence the shrinkage and porosity defects will be formed in the casting below the riser.

(3) The prediction of shrinkage and porosity defects in different schemes is confirmed by the experiment. The results show that there is a certain tendency of shrinkage and porosity defects in the vanes, inner and outer rings of the castings of Schemes 1 and 2, additionally, the shrinkage and porosity defects forming in the outer rings and the vanes near the risers are more serious in Scheme 2. The casting in Scheme 3 has basically no shrinkage and porosity defects. Thus, Scheme 3 can be defined as the optimal process scheme with minimum shrinkage tendency by both simulation and experimental results.

References

[1] Liao J H, Bor H Y, Wei C N, et al. Influence of microstructure and its evolution on the mechanical behavior of modified MAR-M247 fine-grain superalloys at 871 °C. Materials Science and Engineering A, 2012, 539: 93–100.

[2] Zhang J, Wang L, Wang D, et al. Recent progress in research and development of nickel-based single crystal superalloys. Acta Metallurgica Sinica, 2019, 55(9): 1077–1094. (In Chinese)

[3] Wei C N, Bor H Y, Chang L. The effects of carbon content on the microstructure and elevated temperature tensile strength of a nickel-base superalloy. Materials Science and Engineering A, 2010, 527: 3741–3747.

[4] Qi H Y, Yang J S, Yang X G, et al. Low-cycle fatigue behavior of a directionally solidified Ni-based superalloy subjected to gas hot corrosion pre-exposure. Rare Metals, 2019, 38(3): 227–232.

[5] Liu L, Huang T, Xiong Y, et al. Grain refinement of superalloy K4169 by addition of refiners: Cast structure and refinement mechanisms. Materials Science and Engineering A, 2005, 394: 1–8.

[6] Zhang Y B, Yang X L, Tang A. Corrosion behavior of nickel-based 718 alloy determined by in situ electrochemical methods at different partial pressures of H_2S in 25wt% NaCl solution at 150 °C. Rare Metals, 2019, 38(9): 855–863.

[7] Xu Z X, Su X L, Xu Q Y, et al. Numerical simulation on vacuum solution heat treatment and gas quenching process of a low rhenium-containing Ni-based single crystal turbine blade. China Foundry, 2016, 13(6): 402–413.

[8] Xu Q Y, Yang C, Yan X W, et al. Development of numerical simulation in nickel-based superalloy turbine blade directional solidification. Acta Metallurgica Sinica, 2019, 55(9): 1175–1184. (In Chinese)

[9] Tian J W, Bu K, Song J H, et al. Optimization of investment casting process parameters to reduce warpage of turbine blade platform in DD6 alloy. China Foundry, 2017, 14(6): 469–477.

[10] Shen Y, Zheng G, Feng C M. Research progress of investment casting technology. Journal of Netshape Forming Engineering, 2019, 11(1): 54–62.

[11] Li Z L, Xiong J C, Xu Q Y, et al. Deformation and recrystallization of single crestal nickel-based superalloys during investment casting. Journal of Materials Processing Technology, 2014, 217: 1–12.

[12] Pattnaik S, Karunakar D B, Jha P K. Developments in investment casting process–A review. Journal of Material Processing Technology, 2012, 212: 2332–2348.

[13] Sabau A S. Alloy shrinkage factors for the investment casting process. Metallurgical and Materials Transactions B, 2006, 37: 131–140.

[14] Lamm M, Singer R F. The effect of casting conditions on the high-cycle fatigue properties of the single-crystal nickel-base superalloy PWA 1483. Metallurgical and Materials Transactions A, 2007, 38(6): 1177–1183.

[15] Liu Y H, Kang M D, Wu Y, et al. Effects of microporosity and precipitates on the cracking behavior in polycrystalline superalloy Inconel 718. Materials Characterization, 2017, 132: 175–186.

[16] Jiang R, Bull D J, Evangelou A, et al. Strain accumulation and fatigue crack initiation at pores and carbides in a SX superalloy at room temperature. International Journal of Fatigue, 2018, 114: 22–33.

[17] Chen Q Z, Jones N, Knowles D M. The microstructures of base/modified RR2072 SX superalloys and their effects on creep properties at elevated temperatures. Acta Materialia, 2002, 50(5): 1095–1112.

[18] Niu J P, Yin D M, Wang L, et al. Investment casting technology for the turbine blade. Special Casting & Nonferrous Alloys, 2019, 39(11): 1226–1229. (In Chinese)

[19] Herlach D M, Eckler K, Karma A, et al. Grain refinement through fragmentation of dendrites in undercooled melts. Materials Science and Engineering A, 2001, 304–306: 20–25.

[20] Fernández M C, Založnik M, Combeau H, et al. Thermo-solutal convection and macrosegregation during directional solidification of TiAl alloys in centrifugal casting. International Journal of Heat and Mass Transfer, 2020, 154: 119698.

[21] Sun Z Z, Hu H, Chen X. Numerical optimization of gating system parameters for a magnesium alloy casting with multiple performance characteristics. Journal of Materials Processing Technology, 2008, 199: 256–264.

[22] Jie Z Q, Zhang J, Huang T W. Effects of grain refinement on cast structure and tensile properties of superalloy K4169 at high pouring temperature. China Foundry, 2016, 13(2): 101–106.

[23] Wang Y, Wu S P, Xue X, et al. The formation mechanism and criterion of linear segregation in ZL205A alloy. Transactions of Nonferrous Metals Society of China, 2014, 24(11): 3632–3638.

[24] Liu M F, Yao Z H, Dong J X. Application status of numerical simulation in precision forming of block casting turbine. Journal of Netshape Forming Engineering, 2021, 13(1): 35–43.

[25] Wang Y, Wu S P, Niu L J, et al. Optimization of low-pressure die casting process parameters for reduction of shrinkage porosity in ZL205A alloy casting using Taguchi method. Proceedings of the Institution of Mechanical Engineers, Part B: Journal of Engineering Manufacture, 2014, 228(11): 1508–1514.

[26] Wei Y P, Yu B, Yang Q Z, et al. Numerical simulation and experimental validation on fabrication of nickel-based superalloy Kagome lattice sandwich structures. China Foundry, 2020, 17(1): 21–28.